

Dirac semimetal and topological phase transitions in $A_3\text{Bi}$ ($A = \text{Na}, \text{K}, \text{Rb}$)

Zhijun Wang,¹ Yan Sun,² Xing-Qiu Chen,² Cesare Franchini,² Gang Xu,¹ Hongming Weng,^{1,*} Xi Dai,¹ and Zhong Fang^{1,†}
¹Beijing National Laboratory for Condensed Matter Physics and Institute of Physics, Chinese Academy of Sciences, Beijing 100190, China
²Shenyang National Laboratory for Materials Science, Institute of Metal Research, Chinese Academy of Sciences, Shenyang 110016, China

(Received 6 March 2012; revised manuscript received 7 May 2012; published 22 May 2012)

Three-dimensional (3D) Dirac point, where two Weyl points overlap in momentum space, is usually unstable and hard to realize. Here we show, based on the first-principles calculations and effective model analysis, that crystalline $A_3\text{Bi}$ ($A = \text{Na}, \text{K}, \text{Rb}$) are Dirac semimetals with bulk 3D Dirac points protected by crystal symmetry. They possess nontrivial Fermi arcs on the surfaces and can be driven into various topologically distinct phases by explicit breaking of symmetries. Giant diamagnetism, linear quantum magnetoresistance, and quantum spin Hall effect will be expected for such compounds.

DOI: [10.1103/PhysRevB.85.195320](https://doi.org/10.1103/PhysRevB.85.195320)

PACS number(s): 73.20.-r, 71.20.-b, 73.43.-f

I. INTRODUCTION

The topological consideration of effective relativistic quantum field theory in three-dimensional (3D) momentum space allows us to classify a quantum vacuum into three distinct classes, namely, that with gap, Fermi surfaces (FSs), and Weyl points.^{1,2} The topological classes with Fermi surface or gap are well known in condensed matters as metals or insulators. The insulators have been further classified into topologically trivial and nontrivial insulators.³⁻⁵ For the latter case, there have been many candidate materials proposed and some of them confirmed by experimental observations.³⁻⁸ The class of compounds with Weyl Fermi points is relatively rare, however the A phase of ^3He ⁹ and some recent proposals¹⁰⁻¹³ have suggested various possibilities. In addition to Weyl Fermi points, as we will demonstrate in this paper, the Fermi surfaces can be further classified^{1,2} and each of them can be realized in condensed matters. On the other hand, given those known realizations of distinct topological states, it is yet challenging to have a well-controlled example near the phase boundary so that various topological phase transitions can be studied systematically within one system. This challenge becomes further relevant because the vacuum of the Standard Model is regarded to be at the phase boundary with marginal Fermi points (MFPs), which is composed of two overlapping Weyl points with opposite chirality (or topological charge), i.e., forming 3D massless Dirac points.^{1,2} The Weyl points with opposite chirality are stable topological objects only when they are separated. If they meet in momentum space, their topological charges may cancel each other and open a gap. In principle, we may accidentally obtain 3D Dirac points by finely tuning chemical composition or spin-orbit coupling (SOC) strength.¹⁴⁻¹⁷ Unfortunately, such realizations are too fragile and hard to control. In fact, in the presence of crystal symmetry, the 3D Dirac points can be protected and stabilized, as has been discussed in Ref. 18 and will be addressed in this paper.

Here, we report that the 3D Dirac semimetal (or MFP) state can be achieved in a simple stoichiometry compound $A_3\text{Bi}$ ($A = \text{Na}, \text{K}, \text{Rb}$), where the low-energy states form an effective 3D massless gas of Dirac fermions, being different from those in graphene [two-dimensional (2D) Dirac fermion] and Weyl semimetals (nonoverlapping Weyl points). This state is located at the phase boundary and is stabilized by the crystal symmetry. It can be driven into various topologically distinct

phases by explicit breaking of symmetries and thus provides us a nice example for the systematical studies of topological phase transitions. In addition, the state itself is topologically nontrivial in the sense that it has Fermi arcs on the surfaces, and it shows giant diamagnetism and quantum magnetoresistance (MR) in the bulk. It can also show the quantum spin Hall effect in its quantum-well (or thin-film) structure. We will start from the structure and methods in Sec. II, present the main results in Sec. III, and finally conclude in Sec. IV.

II. CRYSTAL STRUCTURE AND METHODOLOGY

Among the alkali pnictides A_3B ($A = \text{alkali metal}, B = \text{As}, \text{Sb}, \text{or Bi}$), $A_3\text{Sb}$ is well known for its application as a photocathode material,¹⁹ but the physical properties of $A_3\text{Bi}$ are not widely studied.²⁰ Both Li_3Bi and Cs_3Bi crystallize in cubic $Fm\bar{3}m$ structure, while Na_3Bi , K_3Bi , and Rb_3Bi are in hexagonal $P6_3/mmc$ phase (or D_{6h}^4 , shown in Fig. 1),²¹ which are our main focus here. Taking Na_3Bi as an example, in this structure,²² there are two nonequivalent Na sites [Na(1) and Na(2)]. Na(1) and Bi form simple honeycomb lattice layers which stack along the c axis, while Na(2) atoms are inserted between the layers, making connection with Bi atoms. From the ionic picture, due to the closed-shell configuration where the number of valence electrons ($3 \times \text{Na-}s^1 + \text{Bi-}p^3$) is equal to six, we may expect a semiconducting nature of these compounds, similar to Na_3Sb .²³ However, they are in fact different.

To explore the electronic properties of $A_3\text{Bi}$, we performed band-structure calculations based on the plane-wave ultrasoft pseudopotential method, using the generalized gradient approximation (GGA) for the exchange-correlation functional. The calculations based on hybrid function (HSE)²⁴ are further supplemented to check the band gap. The cutoff energy for wave-function expansion is 25 Ry, and the k -point sampling grid is $12 \times 12 \times 6$. The experimental lattice parameters²² are used in calculation and convergency is checked with the above settings. The projected surface states are obtained from the surface Green's function of the semi-infinite system, similar to the method used for Bi_2Te_3 and Bi_2Se_3 .^{6,15} For this purpose, the maximally localized Wannier functions from the first-principles calculations have been constructed.

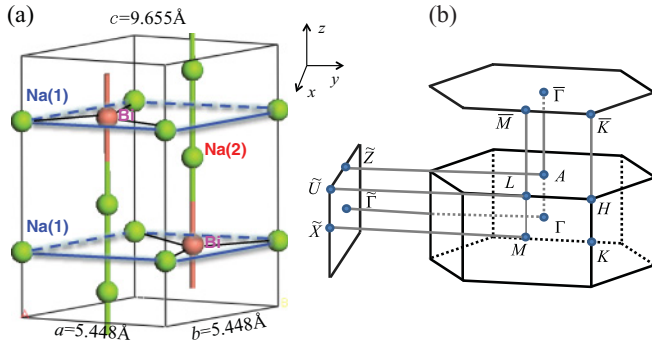


FIG. 1. (Color online) (a) Crystal structure of Na₃Bi with $P6_3/mmc$ symmetry. Na(1) is at $2b$ position $\pm(0, 0, \frac{1}{4})$, and Bi is at $2c$ position $\pm(\frac{1}{3}, \frac{2}{3}, \frac{1}{4})$. They form honeycomb lattice layers. Na(2) is at $4f$ position $\pm(\frac{1}{3}, \frac{2}{3}, u)$ and $\pm(\frac{2}{3}, \frac{1}{3}, \frac{1}{2} + u)$ with $u = 0.583$, threading Bi along the c axis. (b) Brillouin zone of bulk and the projected surface Brillouin zones of (001) and (010) planes.

III. RESULTS AND DISCUSSIONS

A. Electronic structures: Fermi points and Fermi arcs

The calculated electronic structures shown in Fig. 2 suggest that the valence and conduction bands are dominated by Bi- $6p$ and Na- $3s$ states. Very close to the Fermi level, the top valence band is mostly from Bi- $6p_{x,y}$ states, while the conduction band with very strong dispersion is mostly from Na(1)- $3s$ states. All these pictures are similar to that of Na₃Sb,²³ but with the key difference that at the Γ point the Na- $3s$ band

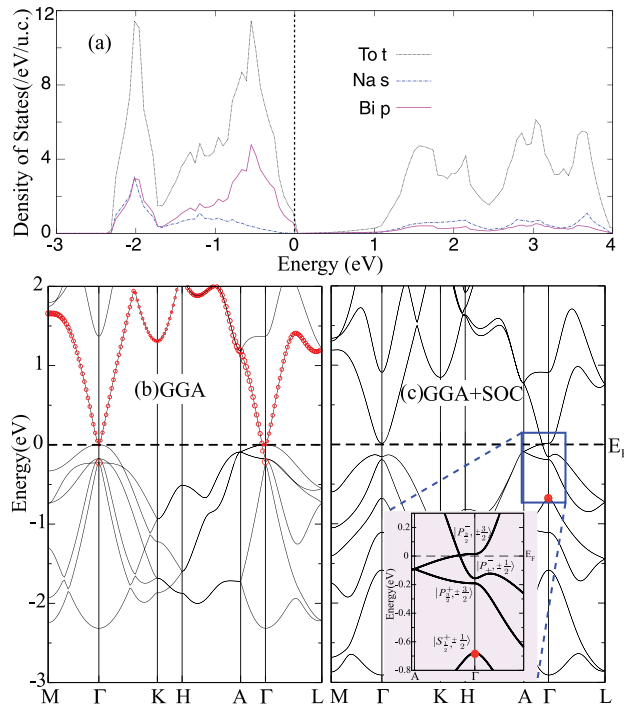


FIG. 2. (Color online) The calculated electronic structures of Na₃Bi. (a) The total and partial density of states. (b) and (c) The band structures without and with spin-orbit coupling, respectively. The red circles indicate the projection to the Na- $3s$ states. The orbital characters of wave functions at the Γ point are labeled in the inset (see Sec. III B for details).

is lower than Bi- $6p_{x,y}$ by about 0.3 eV, and it is further enhanced to be 0.7 eV in the presence of SOC, resulting in a metal with an inverted band structure, rather than the normal narrow gap semiconductor like Na₃Sb.²³ The band inversion is mostly due to the heavier Bi, which has higher $6p$ states and larger SOC compared to Sb. Considering the possible underestimation of the band gap by GGA, the band inversion can be further confirmed by the following evidences: (1) calculation using hybrid functional HSE gives a band inversion around 0.5 eV, still reasonably strong; and (2) the earlier calculations for normal semiconductor K₃Sb²⁵ suggest that its experimental gap can be reasonably reproduced by GGA. With the same method, we calculate the band structures for K₃Bi and Rb₃Bi and find that the band inversions are 0.33 and 0.42 eV, respectively. Because of the similar band structures and the same outcomes of the analysis, we mainly investigate Na₃Bi for details in the following.

Having the inverted band structure, however, Na₃Bi is not gapped, different from topological insulators like Bi₂Te₃ and Bi₂Se₃.⁶ It is a semimetal with two nodes (band crossings) exactly at the Fermi level (Fig. 2). In other words, its Fermi surface consists of two isolated Fermi points, which are located at $(0, 0, k_z^c \approx \pm 0.26 \times \frac{\pi}{c})$ along the Γ -A line. Since both time-reversal and inversion symmetries are present, there is four-fold degeneracy at each Fermi point, around which the band dispersions can be linearized, resulting in a 3D massless Dirac semimetal. It is different from that in graphene not only in dimensionality, but also in its robustness, because the Fermi points here survive in the presence of SOC. This fact also makes a difference from other proposals.^{26,27}

The 4×4 Dirac fermion here is massless because the two bands which cross each other along the Γ -A line belong to different irreducible representations under threefold rotational symmetry. Breaking of this symmetry will introduce interaction between them and make the system insulating. For example, 1% compression along the y axis will open up a gap of ≈ 5.6 meV. This insulating state, however, is topologically nontrivial with $Z_2 = 1$ ^{3,4} due to the inverted band structure around the Γ point. This fact makes Na₃Bi unique, because both bulk 3D Dirac points and nontrivial surface states (a single pair) should coexist (see Fig. 3) as long as the crystal symmetry stands. Furthermore, the surface states are different from that of topological insulators,⁶ in the sense that their Fermi surfaces has Fermi arc structures. As shown in Fig. 3(b) for the [010] surface of stoichiometry Na₃Bi, although the entire Fermi surface is closed, its derivative and Fermi velocity are ill defined at the two singular points (corresponding to the projection of bulk Dirac points to the surface). The spin texture of surface states has a helical structure (also similar to topological insulators), but the magnitude of spin vanishes at the singular points. This kind of Fermi surface has never been found before, and it can be understood following the discussions for Weyl semimetal.^{10,11} If we split the 4×4 Dirac point into two separated 2×2 Weyl points in momentum space by breaking time-reversal or inversion symmetry,^{12,13} the Fermi surface of surface states will also split into open segments which are Fermi arcs discussed in Weyl semimetal [as shown in Fig. 3(d)].^{10,11} All these characters in contrast to conventional metals and topological insulators should be experimentally measurable by modern

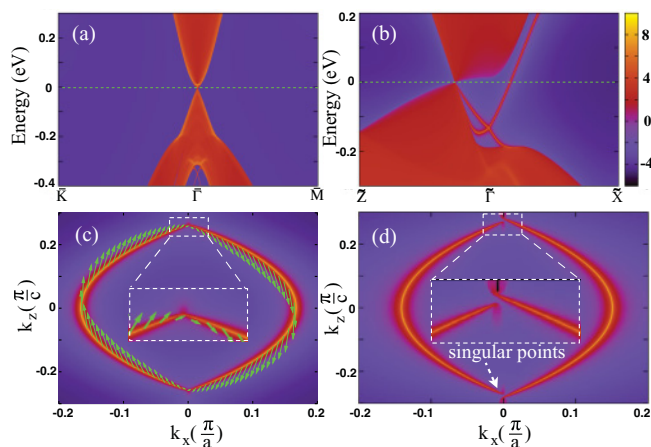


FIG. 3. (Color online) The projected surface states and their Fermi surfaces of Na_3Bi . (a) and (b) The projected surface density of states for [001] and [010] surfaces, respectively. (c) The Fermi surfaces (Fermi arcs) and their spin textures (in-plane components) for the [010] surface states. (d) The Fermi arcs of the [010] surface obtained from the fitted effective Hamiltonian with additional exchange field $h_1 = 6$ meV (see Sec. III C for details). The discontinuity around the singular Fermi points becomes now obvious (enlarged in the insets).

angle-resolved photoemission spectroscopy technique. Our further calculations for K_3Bi and Rb_3Bi suggest that they have qualitatively the same physics as Na_3Bi does.

B. Effective Hamiltonian

The low-energy effective Hamiltonian is derived from the theory of invariants in a similar way as for Bi_2Se_3 , Bi_2Te_3 , and Sb_2Te_3 .²⁸ The first-principles calculations indicate that the wave functions of low-energy states at the Γ point are mostly from the Na-3s and Bi-6 $p_{x,y,z}$ orbitals. For the low-energy Na-3s states at Γ , about 65% of them are from Na(1)-3s and 35% are from Na(2)-3s. Since the system has inversion symmetry, we can start from the bonding and antibonding states of the above relevant orbitals with definite parity:

$$|S^\pm\rangle = \frac{1}{\sqrt{2}}(|\text{Na}, s\rangle \pm |\text{Na}', s\rangle),$$

$$|P_\alpha^\pm\rangle = \frac{1}{\sqrt{2}}(|\text{Bi}, p_\alpha\rangle \mp |\text{Bi}', p_\alpha\rangle),$$

where Na(Bi) and Na'(Bi') are related by inversion symmetry. The superscript \pm indicates the parity, and α is p_x , p_y , or p_z . The bonding and antibonding splittings of these states can be easily seen from the band structure along path A- Γ shown in Fig. 2.

By including the SOC effect in the above atomic picture, spin and orbital angular momentum are coupled and the new eigenstates with definite total angular momentum can be written as $|S_{\frac{3}{2}}^\pm, \pm\frac{1}{2}\rangle$, $|P_{\frac{3}{2}}^\pm, \pm\frac{3}{2}\rangle$, $|P_{\frac{3}{2}}^\pm, \pm\frac{1}{2}\rangle$, $|P_{\frac{1}{2}}^\pm, \pm\frac{1}{2}\rangle$, where the subscript indicates the total angular momentum J . Different from the case with zinc-blende structure (such as HgTe), here the heavy-hole state $|P_{\frac{3}{2}}^\pm, \pm\frac{3}{2}\rangle$ and light-hole state $|P_{\frac{1}{2}}^\pm, \pm\frac{1}{2}\rangle$ are no longer degenerated (with the former being higher) at the Γ point, because Bi atoms are sandwiched by Na(2) atoms along

the z axis, and the Bi p_z orbital is lower than $p_{x,y}$ orbitals. Furthermore, under the D_{6h}^4 symmetry, the light-hole state $|P_{\frac{3}{2}}^\pm, \pm\frac{1}{2}\rangle$ and split-off state $|P_{\frac{1}{2}}^\pm, \pm\frac{1}{2}\rangle$ will mix further to form the new eigenstates: $|P_+^\pm, \pm\frac{1}{2}\rangle$ and $|P_-^\pm, \pm\frac{1}{2}\rangle$.²⁸ Nevertheless these mixed states are not relevant to our discussions for the 3D Dirac points. The band inversion and their crossings along the Γ -A line can be described by the four states $|S_{\frac{1}{2}}^+, \pm\frac{1}{2}\rangle$ and $|P_{\frac{3}{2}}^-, \pm\frac{3}{2}\rangle$. Different from Bi_2Se_3 ,²⁸ where all four bases have the same $|J_z| = \frac{1}{2}$, here we have two different values of $\frac{1}{2}$ and $\frac{3}{2}$, respectively. This difference is essential to the existence and stability of 3D Dirac points observed here.

Therefore, an effective 4×4 $k \cdot p$ Hamiltonian using these four states as bases (in the order of $|S_{\frac{1}{2}}^+, \frac{1}{2}\rangle$, $|P_{\frac{3}{2}}^-, \frac{3}{2}\rangle$, $|S_{\frac{1}{2}}^+, -\frac{1}{2}\rangle$, $|P_{\frac{3}{2}}^-, -\frac{3}{2}\rangle$) can be constructed by considering the time-reversal, inversion, and D_{6h}^4 symmetries. The leading-order Hamiltonian around Γ reads

$$H_\Gamma(\mathbf{k}) = \epsilon_0(\mathbf{k}) + \begin{pmatrix} M(\mathbf{k}) & Ak_+ & 0 & B^*(\mathbf{k}) \\ Ak_- & -M(\mathbf{k}) & B^*(\mathbf{k}) & 0 \\ 0 & B(\mathbf{k}) & M(\mathbf{k}) & -Ak_- \\ B(\mathbf{k}) & 0 & -Ak_+ & -M(\mathbf{k}) \end{pmatrix},$$

where $\epsilon_0(\mathbf{k}) = C_0 + C_1k_z^2 + C_2(k_x^2 + k_y^2)$, $k_\pm = k_x \pm ik_y$, and $M(\mathbf{k}) = M_0 - M_1k_z^2 - M_2(k_x^2 + k_y^2)$ with parameters $M_0, M_1, M_2 < 0$ to reproduce band inversion. By fitting the energy spectrum of the effective Hamiltonian with that of the *ab initio* calculation, the parameters in the effective model can be determined. For Na_3Bi , our fitting leads to $C_0 = -0.06382$ eV, $C_1 = 8.7536$ eV \AA^2 , $C_2 = -8.4008$ eV \AA^2 , $M_0 = -0.08686$ eV, $M_1 = -10.6424$ eV \AA^2 , $M_2 = -10.3610$ eV \AA^2 , and $A = 2.4598$ eV \AA . Please note the leading-order term of off-diagonal elements $B(\mathbf{k})$ has to take the high-order form of $B_3k_zk_+^2$ under the threefold rotational symmetry and the opposite parity of $|S\rangle$ and $|P\rangle$ states. Evaluating the eigenvalues $E(\mathbf{k}) = \epsilon_0(\mathbf{k}) \pm \sqrt{M(\mathbf{k})^2 + A^2k_+k_- + |B(\mathbf{k})|^2}$, we get two gapless solutions at $\mathbf{k}^c = (0, 0, k_z^c = \pm\sqrt{\frac{M_0}{M_1}})$, which are the two Dirac points discussed above, which are separated along the Γ -A line.

If we only concentrate on the neighborhood of each crossing point \mathbf{k}^c and neglect the high-order terms [i.e., $B(\mathbf{k}) \approx 0$], the linearized Hamiltonian is nothing but 3D massless Dirac fermions. The block-diagonal form allows us to decouple the 4×4 matrix into two 2×2 matrices, which are Weyl fermions with degenerate energy but opposite chirality.¹⁰⁻¹³ The breaking of threefold rotational symmetry, however, will introduce a linear leading-order term of $B(\mathbf{k})$, i.e., $B(\mathbf{k}) = B_1k_z$. In such a case, two Weyl fermions will be coupled together, resulting in massive Dirac fermions with gaps, similar to the case of Bi_2Se_3 or Bi_2Te_3 .^{6,28} Nevertheless, as long as the threefold rotational symmetry survives, the Dirac points here should be stable and protected.

C. Phase diagram and topological phase transitions

Na_3Bi with 3D Dirac points (i.e., the MFP state) is located at the phase boundary and may be driven into various topologically distinct states by explicit breaking of

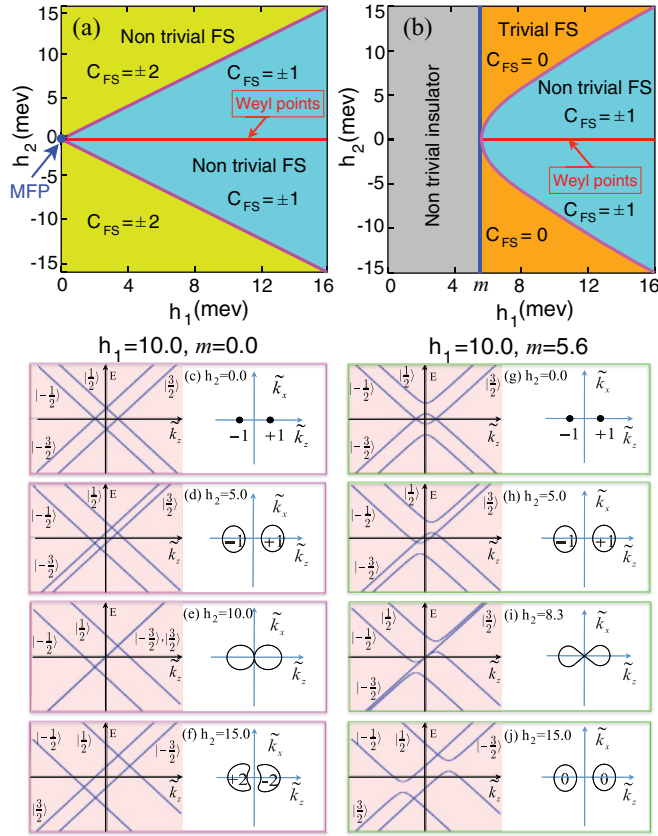


FIG. 4. (Color online) Phase diagrams of Na_3Bi with mass term $m = 0$ meV (left panels) and $m = 5.6$ meV (right panels). The higher-order term of $B(\mathbf{k})$ is neglected for the case of $m = 5.6$ meV. (a) and (b) Phase diagrams. (c) – (j) Band dispersions, corresponding Fermi surfaces, and their topological charges for some characteristic phases (with h_1 fixed to be 10.0 meV). Only the neighborhood around one of the Dirac points is shown with the $\tilde{\mathbf{k}}$ defined as $\mathbf{k} - \mathbf{k}^c$. The $|\pm\frac{1}{2}\rangle$, $|\pm\frac{3}{2}\rangle$ are abbreviations (i.e., J_z values) for the four bases, which are used to indicate the main component of the wave functions for the states away from band crossings (see Sec. III B for details).

symmetries.^{1,2} For simplicity of illustration, here we focus on the effects of exchange interaction. In general, it can be induced by magnetic doping as in diluted magnetic semiconductors²⁹ or by an external field. Other symmetry-breaking terms (such as inversion, mirror, or twofold rotational symmetries of the crystal) may play the similar roles and can be analyzed analogously. Since the $|S\rangle$ and $|P\rangle$ are different orbitals (or pseudospins), we may in general separate any exchange splitting into orbital-dependent and orbital-independent parts as $H_{\text{ex1}} = h_1\sigma_z \otimes \tau_z$ and $H_{\text{ex2}} = h_2\sigma_z \otimes I$, where h_1 and h_2 are field strengths (along the z direction), and $\vec{\sigma}$ and $\vec{\tau}$ are Pauli matrices describing spin and pseudospin, respectively. The total Hamiltonian is given as $H = H_\Gamma + H_{\text{ex1}} + H_{\text{ex2}}$, and the resulting phase diagram is shown in Fig. 4.

If the threefold rotational symmetry of crystal is preserved [i.e., $B(\mathbf{k}) = B_3k_z^c k_+^2$, see left panels of Fig. 4], starting from the MFP state ($h_1 = 0$, $h_2 = 0$), the state with Weyl points will be introduced by h_1 (the horizontal axis), because such an exchange field will split the Dirac point into two separated Weyl points in momentum space. If the h_2 is further introduced,

however, the two Weyl points will separate energetically, and a system with Fermi surfaces (FS) will be obtained. On the other hand, if the threefold rotational symmetry is broken, a mass term $m \approx B_1k_z^c$ will be induced as the leading-order term of $B(\mathbf{k})$. For example, m can be estimated to be the gap size (5.6 meV) at \mathbf{k}^c when 1% compression along the y axis is applied. Then the high-order term of $B(\mathbf{k})$ can be neglected, and a topologically nontrivial insulating phase is obtained (see right panels of Fig. 4). In such a case, the Weyl semimetal phase can be driven only when h_1 is larger than the mass term m .

The FS states can be further classified according to the topological charge (or Chern number C_{FS}) enclosed by the FS. C_{FS} is defined as the net flux of the Berry phase gauge field penetrating the Fermi surface:

$$C_{\text{FS}} = \frac{1}{2\pi} \int_{\text{FS}} [\nabla_{\mathbf{k}} \times \mathbf{A}(\mathbf{k})] \cdot d\mathbf{S},$$

where the integrand is the Berry curvature, $\mathbf{A}(\mathbf{k}) = -i\langle u_{\mathbf{k}} | \nabla_{\mathbf{k}} | u_{\mathbf{k}} \rangle$ is the adiabatic Berry connection for the states $|u_{\mathbf{k}}\rangle$ at the Fermi level, and $d\mathbf{S}$ points from low to high energy. For the case $m = 5.6$ meV (right panels), the two distinct FS states, trivial ($C_{\text{FS}} = 0$) and nontrivial ($C_{\text{FS}} = \pm 1$), are separated by the line defined as $h_1^2 - h_2^2 = m^2$. If $m = 0$ (left panels), both FS states are nontrivial, but with different topological charges ($C_{\text{FS}} = \pm 1$ or ± 2). The appearance of the $C_{\text{FS}} = \pm 2$ phase in this case is due to the $B_3k_zk_+^2$ term of $B(\mathbf{k})$. At the boundary between distinct FS states, the Fermi-surface spheres should be connected, and the C_{FS} becomes ill defined. The nontrivial FS states may become important for the topological superconductivity.³⁰

D. Expected distinct physical properties

Even without the exchange splitting, we can expect some particular physical properties for such compounds. First of all, we will expect the quantum spin Hall effect in z -oriented Na_3Bi thin film (or a $\text{Na}_3\text{Bi}/\text{Na}_3\text{Sb}$ quantum well). Due to the quantum size effect, the k_z is further quantized, and in general the 2D band structures of Na_3Bi thin film will be fully gapped. Then, depending on the number of band inversions associated with the sub-bands, the system should cross over between trivial and nontrivial 2D insulators oscillatorily as a function of film thickness.³¹ Our estimated first critical thickness of Na_3Bi is 35 Å, below (above) which the film is a trivial (nontrivial) insulator. Second, we will expect giant diamagnetism of the 3D massless Dirac fermion.³² The diamagnetic susceptibility, $\chi(\varepsilon) \sim \log\frac{1}{\varepsilon}$, should diverge logarithmically when the chemical potential approaches the 3D Dirac points (i.e., $\varepsilon \sim 0$),³² much stronger than that in narrow gap semimetals like Bismuth. In fact, early experimental measurement had found distinct diamagnetism in the A_3Bi system.³³ Third, we will also expect linear quantum magnetoresistance (MR) as proposed by A. A. Abrikosov.³⁴ In conventional metals with closed Fermi surfaces, the MR should behave quadratically at a low field and saturate at a high field. However, for the 3D massless Dirac fermionic gas, the MR will have linear field dependence if only the lowest Landau level is occupied. This idea has been examined for the Ag_2Te both

experimentally and theoretically,^{34,35} where the Dirac-type energy dispersion is not obvious. Having Na₃Bi with 3D Dirac points, it will be straightforward to check the quantum MR proposal.³⁴

IV. CONCLUSION

In summary, based on the first-principles calculations and effective model analysis, we have shown that the long-pursuing examples with bulk 3D Dirac points can be actually realized in existing compounds A₃Bi (A = Na, K, Rb). It is important to note that this state and its Dirac points are protected by crystal symmetry and therefore stable. We have demonstrated that this state is located at the topological phase boundary and can be driven into various topologically distinct phases, such as topological insulator, topological metal (with nontrivial Fermi

surfaces), and Weyl semimetal states, by explicit breaking of symmetries. It therefore may provide us a condensed-matter simulator of the Standard Model, from the viewpoint of an emerging relativistic quantum field at low energy. In addition, we have shown that the state itself is unconventional in the sense that it shows Fermi arcs on the surface, giant diamagnetism and linear quantum magnetoresistance in the bulk, and quantum spin Hall effect in the quantum-well or thin-film structure. Experimenters are strongly encouraged to test those proposals and phenomena.

ACKNOWLEDGMENTS

We acknowledge support from NSF of China, the 973 program of China, and the Hundred Talents Project of the Chinese Academy of Sciences.

*hmweng@aphy.iphy.ac.cn

†zfang@aphy.iphy.ac.cn

¹F. R. Klinkhamer and G. E. Volovik, *Int. J. Mod. Phys. A* **20**, 2795 (2005).

²Grigory E. Volovik, *The Universe in a Helium Droplet* (Clarendon Press, Oxford, 2003).

³M. Z. Hasan and C. L. Kane, *Rev. Mod. Phys.* **82**, 3045 (2010).

⁴X.-L. Qi and S.-C. Zhang, *Rev. Mod. Phys.* **83**, 1057 (2011).

⁵A. P. Schnyder, S. Ryu, A. Furusaki, and A. W. W. Ludwig, *Phys. Rev. B* **78**, 195125 (2008).

⁶H. J. Zhang, C. X. Liu, X. L. Qi, X. Dai, Z. Fang, and S. C. Zhang, *Nat. Phys.* **5**, 438 (2009).

⁷Y. Xia, D. Qian, D. Hsieh, L. Wray, A. Pal, H. Lin, A. Bansil, D. Grauer, Y. S. Hor, R. J. Cava, and M. Z. Hasan, *Nat. Phys.* **5**, 398 (2009).

⁸Y. L. Chen, J. G. Analytis, J.-H. Chu, Z. K. Liu, S.-K. Mo, X. L. Qi, H. J. Zhang, D. H. Lu, X. Dai, Z. Fang, S. C. Zhang, I. R. Fisher, Z. Hussain, and Z.-X. Shen, *Science* **325**, 178 (2009).

⁹A. J. Leggett, *Rev. Mod. Phys.* **47**, 331 (1975).

¹⁰X. G. Wan, A. M. Turner, A. Vishwanath, and S. Y. Savrasov, *Phys. Rev. B* **83**, 205101 (2011).

¹¹G. Xu, H. M. Weng, Z. J. Wang, X. Dai, and Z. Fang, *Phys. Rev. Lett.* **107**, 186806 (2011).

¹²A. A. Burkov and L. Balents, *Phys. Rev. Lett.* **107**, 127205 (2011).

¹³A. A. Burkov, M. D. Hook, and L. Balents, *Phys. Rev. B* **84**, 235126 (2011).

¹⁴S. Murakami, *New J. Phys.* **9**, 356 (2007).

¹⁵W. Zhang, R. Yu, H. J. Zhang, X. Dai, and Z. Fang, *New J. Phys.* **12**, 065013 (2010).

¹⁶S. Y. Xu, Y. Xia, L. A. Wray, S. Jia, F. Meier, J. H. Dil, J. Osterwalder, B. Slomski, A. Bansil, H. Lin, R. J. Cava, and M. Z. Hasan, *Science* **332**, 560 (2011).

¹⁷T. Sato, K. Segawa, K. Kosaka, S. Souma, K. Nakayama, K. Eto, T. Minami, and Y. Ando, *Nat. Phys.* **7**, 840 (2011).

¹⁸S. M. Young, S. Zaheer, J. C. Y. Teo, C. L. Kane, E. J. Mele, and A. M. Rappe, *Phys. Rev. Lett.* **108**, 140405 (2012).

¹⁹S. H. Wei and A. Zunger, *Phys. Rev. B* **35**, 3952 (1987).

²⁰M. Tegze and J. Hafner, *J. Phys.: Condens. Matter* **4**, 2449 (1992).

²¹T. B. Massalski, *Binary Alloy Phase Diagrams* (ASM, Materials Park, 1990).

²²G. Brauer and E. Zintl, *Z. Phys. Chem., Abt. B* **37**, 323 (1937).

²³A. R. H. F. Ettema and R. A. de Groot, *Phys. Rev. B* **61**, 10035 (2000).

²⁴J. Heyd, G. E. Scuseria, and M. Ernzerhof, *J. Chem. Phys.* **124**, 219906 (2006).

²⁵A. R. H. F. Ettema, R. A. de Groot, *J. Phys.: Condens. Matter* **11**, 759 (1999).

²⁶H. Kino and T. Miyazaki, *J. Phys. Soc. Jpn.* **75**, 034704 (2006).

²⁷V. Pardo and W. E. Pickett, *Phys. Rev. Lett.* **102**, 166803 (2009).

²⁸C. X. Liu, X. L. Qi, H. J. Zhang, X. Dai, Z. Fang, and S. C. Zhang, *Phys. Rev. B* **82**, 045122 (2010).

²⁹R. Yu, W. Zhang, H. J. Zhang, S. C. Zhang, X. Dai, and Z. Fang, *Science* **329**, 61 (2010).

³⁰X. L. Qi, T. L. Hughes, and S. C. Zhang, *Phys. Rev. B* **81**, 134508 (2010).

³¹C. X. Liu, H. J. Zhang, B. H. Yan, X. L. Qi, T. Frauenheim, X. Dai, Z. Fang, and S. C. Zhang, *Phys. Rev. B* **81**, 041307 (2010).

³²M. Koshino and T. Ando, *Phys. Rev. B* **81**, 195431 (2010), and see references therein.

³³E. Röber, K. Hackstein, H. Coufal, and S. Sotier, *Phys. Status Solidi B* **93**, K99 (1979); K. Hackstein, S. Sotier, and E. Lüscher, *J. Phys. Colloques* **41**, C8-49 (1980).

³⁴A. A. Abrikosov, *Phys. Rev. B* **58**, 2788 (1998), and see references therein.

³⁵W. Zhang, R. Yu, W. Feng, Y. Yao, H. M. Weng, X. Dai, and Z. Fang, *Phys. Rev. Lett.* **106**, 156808 (2011).